Polymer 50 (2009) 5084–5093

Contents lists available at ScienceDirect

Polymer

journal homepage: www.elsevier.com/locate/polymer

Influence of position and composition on adhesion to injection-molded TPO plaques as model automotive parts

Kangqing Deng [a,b], Neda Felorzabihi [c], Mitchell A. Winnik [b,c,*], Zhaohua Jiang [a,**], Zhihui Yin [b], Yuanqin Liu [b], Philip V. Yaneff [d], Rose A. Ryntz [e]

[a] Department of Applied Chemistry, Harbin Institute of Technology, Harbin 150001, China
[b] Department of Chemistry, University of Toronto, 80 St. George Street, Toronto, Ontario, Canada M5S 3H6
[c] Department of Chemical Engineering, University of Toronto, 200 College Street, Toronto, Ontario, Canada M5S 3E5
[d] E. I. Dupont Canada, 408 Fairall Street, Ajax, Ontario, Canada L1S 1R7
[e] Visteon Automotive Systems, Dearborn, MI 58121, USA

ARTICLE INFO

Article history:
Received 11 June 2009
Received in revised form
29 July 2009
Accepted 1 August 2009
Available online 20 August 2009

Keywords:
Thermoplastic polyolefin
Chlorinated polyolefin
Adhesion

ABSTRACT

Single lap shear adhesion measurements on model isotactic polypropylene and thermoplastic polyolefin (TPO) substrates which sandwich a chlorinated polyolefin (CPO) show similar values of the fracture strength, as determined from the stress at break, but much larger deformation at break for the substrates that contain a copolymer of ethylene with 9 wt% butane (EBR9) as an impact modifier. We also found for sections cut from a large format (300 × 100 mm) plaque of TPO12 (12 wt% EBR9), that the fracture energy increased as a function of distance from the gate. ATR-FTIR measurements on these sections indicated that there was a variation in the EBR content in the near-surface region of the substrate, and that stronger adhesion correlated with an increase of EBR content at or near the surface.

1. Introduction

Thermoplastic olefins (TPO) refer to a family of blends of isotactic polypropylene (iPP) with various polyolefins such as ethylene copolymers with propylene (EPR), butene (EBR), and others. These polyolefins form a dispersed phase which enhances the physical and mechanical properties of iPP in the solid state [1]. Yokoyama and Ricco [2] found that EBR has a higher toughening efficiency than EPR, and the fracture toughness can be increased by increasing the molecular weight of the dispersed elastomeric phase. These polymers are commonly blended in a high-speed mixer or twin-screw extruder, and the parts are fabricated by injection molding. Because of their lightweight, low cost, good mechanical properties, recyclability, and ease of molding into complex shapes, they have become increasing popular alternatives to steel for applications such as bumpers, fascia, and some interior automotive parts [3].

The majority of plastic automotive parts are painted. The coating serves both a protective and decorative function. Because polypropylene is a non-polar hydrocarbon material with a low surface free energy, it is a great challenge to obtain good adhesion of a coating directly onto a fabricated TPO part [3]. Thus, special surface treatments are necessary to promote adhesion to the TPO surface. These include plasma, flame treatment, and corona discharge which can oxidize the surface and introduce polar functional groups. Another commonly used method for surface preparation is to coat a cleaned TPO surface with a thin layer film of a polymer that can act as an adhesion promoter (AP). The adhesion promoter has to provide both reasonable adhesion to the TPO surface and a surface that can interact strongly with the paint layer. One class of widely used adhesion promoters is the chlorinated polyolefins (CPOs). Although a significant advance has been attained in the development of adhesion promoting polymers with improved performance, paint-adhesion failure, which often occurs on curved surfaces, is still a serious problem in the automotive industry.

Injection-molded polypropylene plaques show a clear two-phase structure of skin and core. Tang and Martin [4] found an iPP-rich layer at the TPO surface and a well-elongated fibrous morphology of the rubber components in the iPP matrix, just below the iPP-rich layer. More details about this type of

* Corresponding author. Department of Chemistry, University of Toronto, Toronto, Canada M5S 3H6.
** Corresponding author. Department of Applied Chemistry, Harbin Institute of Technology, Harbin 150001, China.
E-mail addresses: mwinnik@chem.utoronto.ca (M.A. Winnik), jiangzhaohua@hit.edu.cn (Z. Jiang).

0032-3861/$ – see front matter © 2009 Elsevier Ltd. All rights reserved.
doi:10.1016/j.polymer.2009.08.027

morphology were obtained in a series of Laser Scanning Confocal Fluorescence Microscopy (LSCFM) experiments in which the EBR dispersed phase was labeled with a fluorescent dye [5,6]. One study, which combined polarizing optical microscopy (POM) measurements with LSCFM identified a "fine-grained layer" of impact modifier, in the form of small droplets, beneath a skin layer in which long fibers of EBR were trapped by the shear-induced crystallization of iPP [7].

Ryntz [8,9] developed a hypothesis that the flow fields associated with the injection molding of automotive parts affects not only the morphology of the TPO, but also the morphology at or near the polymer surface. These morphology differences play a crucial role in determining the strength of the interaction with the adhesion promoter. Ryntz [10] has explored this idea by investigating the effect of TPO morphology on subsequent paintability and thermal shock performance. She postulated that the rearrangement of polypropylene crystallites at the uppermost surface of the TPO during a 120 °C annealing step accounts for the increased cohesive strength of the painted composite.

Several studies have attempted to determine the width of the interface between TPO and CPO. Mirabella and Dioh [11] used scanning transmission X-ray microscopy (STXM) to characterize the TPO/CPO interface and found an interface thickness of 340 ± 80 nm. Yin et al. [12] used high-resolution electron microscopy, in conjunction with EDX analysis to determine a somewhat thinner interface. In those studies the interface width found for TPO/CPO was much closer in magnitude to that found for EBR/CPO than for iPP/CPO. This is one of the reasons that many papers suggest that the source of adhesion between CPO and TPO is preferential interaction of the CPO with impact modifier at the TPO surface.

All studies of CPO coated TPO indicate that the presence of impact modifier improves the adhesion between the CPO and TPO. Tomasetti et al. [13] reported that the adhesion of CPO to blends of iPP/EPR was much better than that to iPP itself. Yin et al. [12] examined the adhesion of CPO to a TPO composed of metallocene EBR and iPP. For samples subjected to a "dry" bake at 120 °C, the stress at break was greater for the TPO than for the iPP itself. This situation changed for samples exposed to warm xylene vapors, a model for a wet-on-wet-on-wet coat-and-bake process, where the differences were rather small. Morris et al. [14,15] used confocal Raman microscopy to monitor penetration of their CPO into an EPR–iPP TPO substrate and found that the coating and bake conditions used led to a 20 μm deep penetration of CPO into the TPO.

In this report, we wish to follow up on the studies cited above by comparing the strength of adhesion of CPO with an EBR–iPP TPO as a function of composition, and for larger format injection-molded plaques, as a function of position from the gate. We describe single lap shear measurements coupled with morphology studies, both of the polymer surface before coating and of the exposed surfaces after fracture.

The iPP and EBR samples we employed are the same as those used in the studies reported by Yin et al. [12]. We also compare samples cut from large format injection-molded plaques prepared at Visteon (V-TPO samples) with smaller samples blended and injection-molded individually using a mini-twin-screw extruder at the University of Toronto (UT-TPO samples). In one case, where we detect a variation in adhesion strength with position on a V-series TPO plaque, we also detect by attenuated total reflectance-Fourier transform infrared (ATR-FTIR) small variations in the EBR content in the near-surface regions of the samples. The fracture surface morphology of lap shear joint was examined by polarized optical microscopy (POM), scanning electron microscopy (SEM), and LSCFM.

2. Experimental

2.1. Materials

TPO samples were fabricated with polymers from ExxonMobil. The isotactic polypropylene (iPP, Escorene 1042, Ziegler Natta catalyst) was melt-blended with poly(ethylene-butene) (EBR9, Exact 3125, 9 wt% butene, metallocene catalyst) copolymer. The molecular weight of iPP sample was characterized to be $M_n = 67{,}000$ g/mol with PDI = 3.51 and that of EBR9 to be $M_n = 46{,}000$ g/mol with PDI = 1.96 [12]. TPO12 refers to an iPP-EBR9 blend containing 12 wt% EBR9. TPO25 refers to a similar blend containing 25 wt% EBR9. Two types of injection-molded plaques were examined. One set of samples, with dimensions $300 \times 100 \times 3$ mm^3 were provided by Visteon, which we will refer to as V-TPO. They were prepared by injection molding through a film gate (with the same width as the plaque) at one end of the mold. A second set of samples were prepared in our laboratories by melt-blending the components in a twin-screw mini-extruder (DSM Micro 15, The Netherlands), with a gas-pressure driven injection molding attachment, and extruded through a single strand die. The extruder was run under the following conditions: 190 °C for the near feeder block, 220 °C for the middle block, 230 °C for the near die part and 100 rpm for the screw speed. To ensure uniform blending, samples were cycled through the instrument for 8 min prior to transfer to the injection molder. Each blend was molded into a rectangular plaque ($60 \times 12 \times 2$ mm^3) through a 2.0 mm wide pin gate using a DSM micro-injection molding machine (3.5 cm^3) at 70 psi injection pressure with a mold temperature of 43 °C. These plaques are referred to as UT-TPO.

The chlorinated polypropylene sample employed here (CPO, Superchlon 872S, 21.8 wt% chlorine content, manufacturer's specification) was provided by Nippon Paper Chemicals Co. Ltd. Its molecular weight was determined to be $M_n = 29{,}000$ with PDI = 2.9 by gel permeation chromatography (GPC, polystyrene standards). By titration, it had an anhydride content of 0.18 mmol/g polymer [16]. The CPO samples used in these experiments consisted of a blend of 95 wt% Superchlon 872 plus 5 wt% of a fluorescent dye-labeled sample (CPO-HY, 0.1 mmol dye/g polymer), prepared previously in this laboratory from Superchlon 872 by Ma [16]. The dye-labeled polymer has a maximum absorbance in the UV–Vis spectrum of $\lambda_{max} = 456$ nm, and an emission maximum of $\lambda_{em} = 505$ nm.

2.2. Single lap shear test

The magnitude of the adhesive strength was determined by utilizing a single lap shear test [17]. The lap shear joints were fabricated as follows: a 10 wt% solution of CPO in tetrahydrofuran (THF) was prepared. THF was used as solvent to minimize solvent penetration into the polyolefin plaques. After gently cleaning with acetone, one surface of each iPP or TPO plaque to be tested was spin-coated with the CPO/THF solution at a speed of 1000 rpm. After drying for 30 min at 50 °C, the coated plaques were baked at 120 °C for 20 min to promote adhesion of CPO to the iPP or TPO substrates. This temperature is above the melting temperature (T_m) of the linear EBR9 polymers used as the impact modifiers in our TPO sample, but well below the normal melting temperature (ca. 167 °C) of the iPP matrix. The dry CPO layer had a uniform thickness of about 7–9 μm.

Sandwich-like three-layer samples (iPP/CPO/iPP, TPO/CPO/TPO) were prepared from pairs of CPO coated plaques. To prepare an individual sample, a pair of CPO coated substrates was placed in the appropriate lap shear geometry (Figs. 1 and 2) with the two CPO layers in contact, and then the sandwich sample was heated at

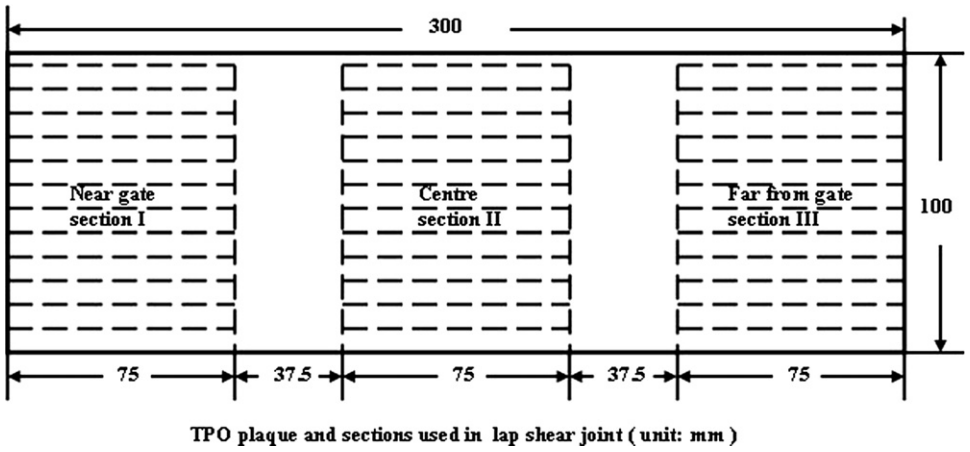

Fig. 1. The dimensions of the TPO plaques provided by Visteon Co. Samples were injected via a film gate whose width was identical to that of the sample. The dashed lines indicate where the plaque was cut to get the rectangle sections. Labels identify sections cut from the plaques for lap shear tests.

100 °C for 4 min in a Carver Press under gentle pressure to make the central CPO layers join well for the lap shear test. The contact dimensions were 6 mm wide × 25 mm long for the V-iPP or V-TPO plaques; and 12 mm wide × 25 mm long for the UT-iPP or UT-TPO. The UT-plaques had the same dimensions as those employed in an earlier study [12]. In the V-iPP and V-TPO samples, where we were interested in the location of the section with respect to the gate, both components of the sandwich were taken from the same part of the plaque. Prior to the lap shear tests, the joints were aged for 17 h at 30 °C in a preheated oven. After removal from the oven, they were allowed to cool to room temperature (ca. 23 °C) and then immediately subjected to shear fracture in the tension mode using an Instron 5543 tester at a crosshead speed of 5 mm/min at room temperature. Force–displacement curves were recorded. At least five specimens of each sample were tested.

The joint strength (τ_f), reported in units of shear stress, was calculated as the ratio of the failure load F_f to the adhesive overlap area A.

$$\tau_f = \frac{F_f}{A} \tag{1}$$

The fracture energy G_c (or adhesion energy) can be obtained directly by T-peel test [18] or by double cantilever beam (DCB) test [19]. Lap shear test can give an estimate of G_c, which can be evaluated as:

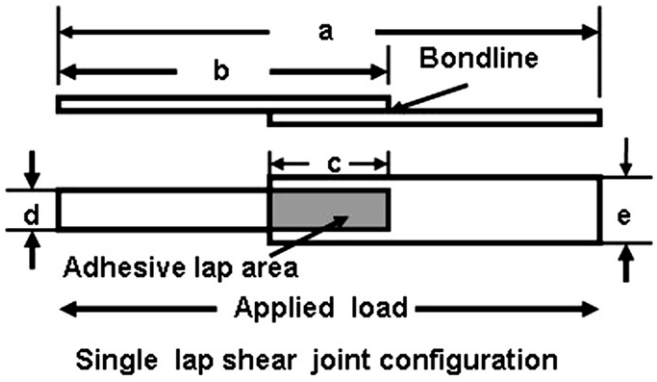

Fig. 2. Single lap shear joint geometry used in this study. The dimensions of the sections cut from the plaques provided by Visteon were: $a = 125$ mm, $b = 75$ mm, $c = 25$ mm, $d = 6$ mm, $e = 7$ mm. The dimensions of the UT-plaques were $a = 95$ mm, $b = 60$ mm, $c = 25$ mm, $d = 12$ mm, $e = 12$ mm.

$$G_c = \int \left(\frac{F}{A}\right) dl \tag{2}$$

where l is the length of the overlap area during lap shear test, and F is the applied load during the lap shear test. Calculations of the fracture energy G_c were carried out as described previously [20].

2.3. ATR-FTIR analysis

Attenuated Total Reflectance-Fourier Transform Infrared (ATR-FTIR) functions by passing a radiation beam through a crystal made of a high-refractive index infrared-transmitting material, which is then totally internally reflected at the surface. In this experiment, a symmetrical trapezoidal ZnSe crystal ($50 \times 20 \times 2$ mm^3, with a refractive index of 2.42, with 45° entrance and exit face angles) was purchased from Harrick Scientific Products, Inc. (Pleasantville, NY 10570). The samples were placed between the ZnSe crystal and a stainless-steel cover (with a rubber support attached) with a variable pressure, to ensure good contact between the sample and the crystal. ATR single-beam reflection spectra were collected with a Spectrum BX FT-IR system: 50 scans with a resolution of 4 cm^{-1} were taken. The ATR spectra were calculated by ratioing the band intensity of the sample spectrum with that of an appropriate reference spectrum, which had been collected by transmittance FTIR. The reference samples adopted in this paper are iPP/EBR blends at ratios of 88/12, 75/25, 50/50, 25/75 (w/w). Absorption values were assigned using peak height measurements. ATR and baseline corrections were made before the peak intensities of the ATR spectra were measured.

2.4. Scanning electron microscope (SEM)

The morphology of skin layer, the surface of the TPO plaques, and the fracture surface morphology of the lap shear test samples were characterized with a Hitachi S-5200 scanning electron microscope, operated at 1.5 kV. TPO plaques were cut into ca. $3 \times 3 \times 0.4$ mm^3 sections and then immersed in xylene solvent for 2.5 h at 99 °C to dissolve away EBR from the plaques. After the solvent-etched plaques were dried in air at 30 °C for at least 2 h, the etched surfaces were examined by SEM.

To observe crystalline structures at or near the surface of the TPO plaques by SEM, samples were stained with ruthenium tetroxide (RuO_4) vapor by suspending them in a closed bottle above an aqueous RuO_4 solution for 24 h.

2.5. Differential scanning calorimetry (DSC)

DSC measurements were carried out with a TA Q-100 DSC instrument. The instrument was calibrated with indium, and nitrogen purge gas was employed. Samples of about 8 mg were encapsulated in aluminum pans and heated from −50 °C to 200 °C and then cooled down to −50 °C at a rate of 10 °C/min. After that, the samples were again heated to 200 °C at the same rate.

The enthalpies of crystallization and melting were obtained by integrating the heat flow curve to a flat baseline. The weight fraction of crystallinity was calculated via the total enthalpy method, according to:

$$X_c = \frac{\Delta H_m}{\Delta H_m^0} \quad (3)$$

where X_c is the fractional crystallinity, ΔH_m is the measured enthalpy of melting, and ΔH_m^0 is the ideal enthalpy of melting for a perfect crystal of the polymer. The known ΔH_m^0 value for PP is 209 J/g and for PE is 281 J/g [21]. Thus, we found that the X_c of iPP, EBR and CPO were 44.9%, 30.8% and 7.2%, respectively.

2.6. Laser scanning confocal fluorescence microscopy (LSCFM)

The fracture surface morphology of individual iPP/CPO/iPP and TPO/CPO/TPO sandwich samples was visualized using a Leica TCS SP2 laser scanning confocal fluorescence microscope system fitted with a dry objective. An argon ion laser (100 mW JDS Uniphase) generated the excitation light, $\lambda_{ex} = 488$ nm. With a band-pass filter, the emission from the samples was collected over the range of $\lambda_{em} = 493$–560 nm. The pinhole was set at 100 μm, resulting in a focal plane depth less than 0.6 μm thick.

2.7. Polarized optical microscopy (POM)

Optical micrographs were taken with an Olympus-BH2-UMA microscope equipped with polarizers. The skin layer of TPO plaques was observed under crossed polarizers at a magnification of 100×. The surfaces of iPP plaques, TPO plaques and CPO adhesive coated onto TPO plaques were observed under crossed polarizers at a magnification of 50×. After lap shear tests, the fracture surfaces of the lap shear test samples were analyzed under crossed polarizer at a magnification of 50×.

3. Results and discussion

3.1. Single lap shear test results

To measure the strength of adhesion of CPO to iPP and to TPO, we carried out lap shear measurements. The iPP and TPO samples were spin-coated with solutions of CPO in THF. The thickness of the CPO layer was estimated by LSCFM operated in the z-scan mode. This non-destructive optical sectioning technique generates an image corresponding to a cross section of the sample in which the bright area represents the dye-labeled CPO. Examples are presented in (Fig. S1, Supporting Information). The CPO layers were uniform for individual samples, with thicknesses of 7–9 μm.

One would also like to have a non-destructive means for measuring the thickness of the CPO layer in these lap shear sandwich samples, but this turned out not to be possible. The problem for LSCFM was that the iPP and TPO substrates were too turbid to allow light penetration to the depth of the CPO layer. In an attempt to overcome this problem, model samples were prepared and then cut by hand with a razor blade (for details, see Supporting Information and Fig. S2) to reduce the thickness of one of the substrates. In this way, z-scans indicated that the CPO layer in the lap shear sandwich was on the order of 12–15 μm thick.

Lap shear measurements were carried out with these various sandwich samples. For both the V-series and UT-series, we examined both fracture strength (tensile stress at break) and adhesion energy G_c as a function of EBR content in the samples. The adhesion energy is the integrated area under the stress–strain curves. For a selected set of V-series plaques, we also examined these properties as a function of the distance of the sample from the gate. One set of experimental results is presented in Fig. 3A. These experiments compare center-cut sections of V-series plaques, comparing iPP, TPO12 and TPO25. One can see that the tensile stress at break is rather similar for each of the samples, irrespective of the substrate. In contrast, the extension-to-break is much greater for the TPO samples than for the iPP samples. There is also an indication of a greater extension-to-break for the samples with the higher EBR content, which for TPO25 is accompanied by a somewhat reduced tensile stress at break.

In Fig. 3B, we see that one sample of V-TPO12 showed a significant variation of the strain at break with the distance from the gate. We will examine the origin of this effect in a later section of this paper.

The data on fracture strength and adhesion energy as a function of composition is summarized in Fig. 4. In the upper line in Fig. 4A for the V-series samples, one sees that the tensile stress at break is not very sensitive to the EBR content. Each data point represents an average of measurements on 5 samples taken from the center part of the plaque. There are some suggestions that fracture strength is

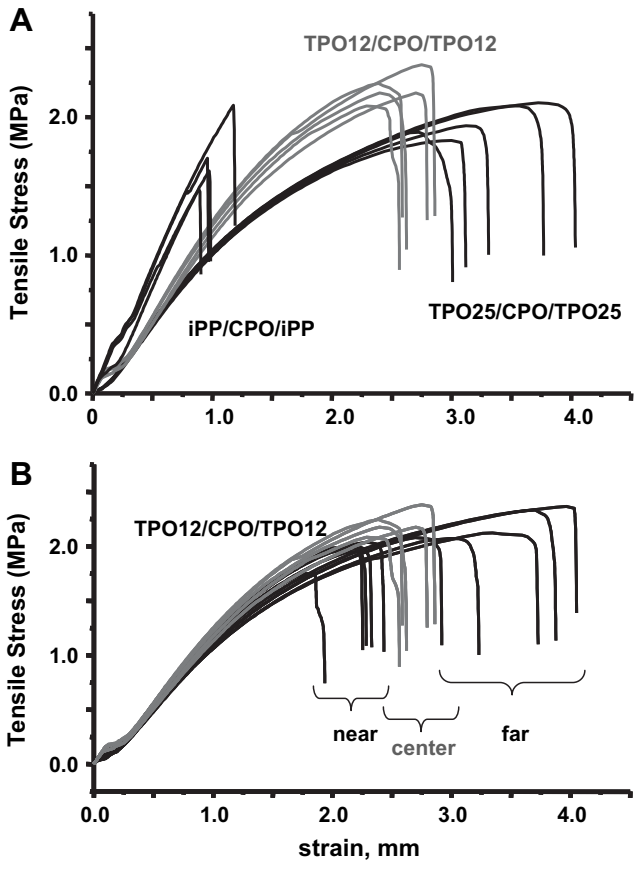

Fig. 3. Lap shear measurements (5 samples each) on V-iPP/CPO/iPP and V-TPO/CPO/TPO samples. A). One set of measurements comparing center-cut sections of iPP, TPO12, and TPO25 plaques. B). One set of samples from a V-TPO12 plaque with a pronounced difference in adhesion energy as a function of distance from the gate.

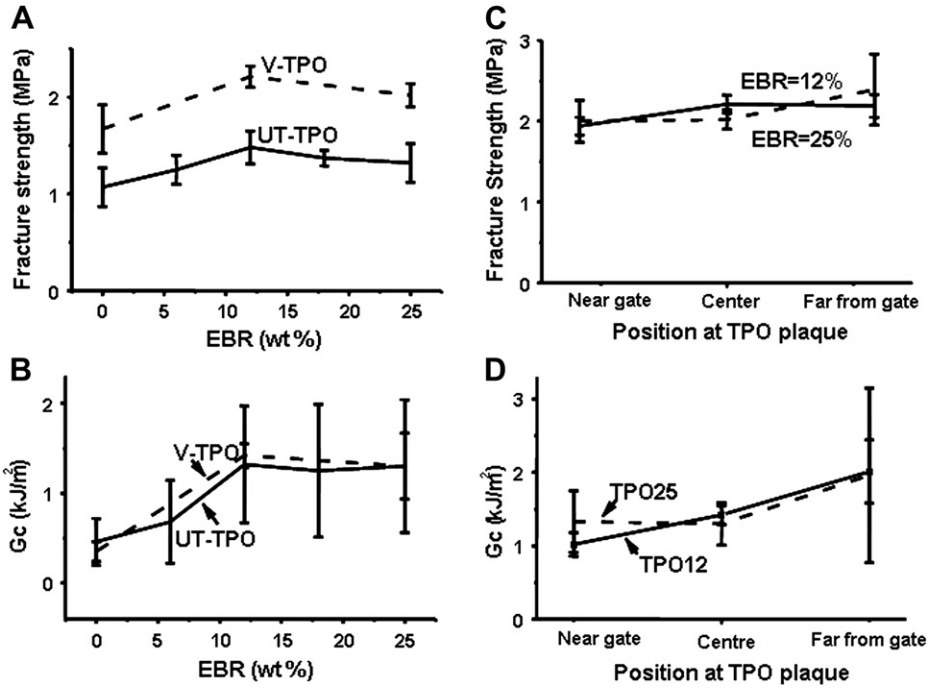

Fig. 4. Fracture strength at break (A and C) and adhesion energy (B and D) for V-TPO and UT-TPO samples measured by lap shear experiments.

greater for the two TPO samples than for iPP, but the difference is small. This figure also shows that there was a significant difference in the fracture strength of the V-series and UT-series plaques. For all compositions, the UT specimens fracture at lower fracture strength than the V-series plaques.

In Fig. 4B, one sees that the adhesion energy for both the V-series and UT-series samples is sensitive to the EBR content. The adhesion energy increased with increasing EBR9 content in TPO plaques until the adhesion energy reached its maximum at an EBR9 content of about 12 wt%. Beyond this content, the adhesion energy remained unchanged. Fig. 4B also shows that there was almost no difference in the adhesion energy of the V-series and UT-series plaques.

In Fig. 4C, it can be observed that the fracture strength for TPO12 and TPO25 plaques is not very sensitive to the position at TPO plaques, which shows only a small increase in fracture strength from near the gate to far from the gate. However, in Fig. 4D, for a V-TPO12 plaque, there is a more obvious increase in adhesion energy from near the gate to far from the gate. Fig. 4 also shows that the adhesion energy determined from the lap shear tests is more sensitive to EBR9 content in the TPO plaques and gate position than fracture strength. We conclude that adhesion energy is a better parameter to characterize the adhesion property of such samples. The overall finding that the strength of adhesion between CPO and TPO increases with the impact modifier content of the TPO is consistent with the results reported previously by Tomasetti et al. [13] and Yin et al. [12].

3.2. Morphology of the surface and skin layer of TPO plaque

Injection-molded polypropylene typically shows a clear two-phase structure consisting of a skin layer and a core when its cross sections are observed with a polarizing microscope. The skin layer consists of a highly birefringent region, which is very different from the spherulite crystals found in core (bulk) [22]. The skin layer is formed through shear-induced crystallization in the surface region of the mold. The thickness of the skin layer varies widely with the kind of resin and the molding conditions, as well as with the physical properties of the sample such as the elastic modulus, the yield strength, and the extent of mold shrinkage. Matsumoto et al. [23] found that the thickness of these oriented layers was governed mainly by resin temperature and mold temperature. Fujiyama and Wakino [24,25] found that the skin layer of iPP under their injection molding conditions was about 600 μm thick.

Ryntz et al. [26] examined the nature of the skin layer of TPO plaques very similar to the V-TPO plaques examined here. Values of the skin layer thickness ranged from about 240 to 460 μm. They reported that the thickness of the skin layer of iPP was greater than that of TPO, and the thickness of the skin layer of both iPP and TPO plaques deceased from near gate to far from the gate. We obtained similar values, as shown in Table 1.

Among the features that one expects to affect the adhesion properties of CPO to TPO plaques are the surface and the near-surface morphology of the TPO. The morphological changes at and near the surface of TPO affect the adhesion to the substrate [10]. Here we examine the surface morphology of our samples by SEM, employing both solvent etching and RuO_4 staining to generate contrast. For solvent etching, thin sections of TPO plaques were exposed to warm xylene (99 °C) to dissolve selectively the EBR component. The voids seen in the SEM images should indicate the location of the dissolved component. Fig. 5a–c presents SEM images of the surfaces of a V-TPO25 sample after the EBR was extracted, cut from different positions in the plaques. The inset of Fig. 5b shows

Table 1
Near-surface properties of V-iPP and V-TPO plaques.[a]

Plaque	T_m^a, °C		Skin layer thickness[b] (μm)		
	iPP	EBR	Near gate	Center	Far from gate
iPP	167.4	–	460	450	270
TPO12	165.2	106.3	370	370	270
TPO25	166.4	106.6	390	380	240

[a] The melting temperature of skin was obtained as the peak of the melting endotherm from the first scan of a DSC measurement under N_2 at 10 °C/min from thin sections cut from the surface of the samples.
[b] From POM measurements.

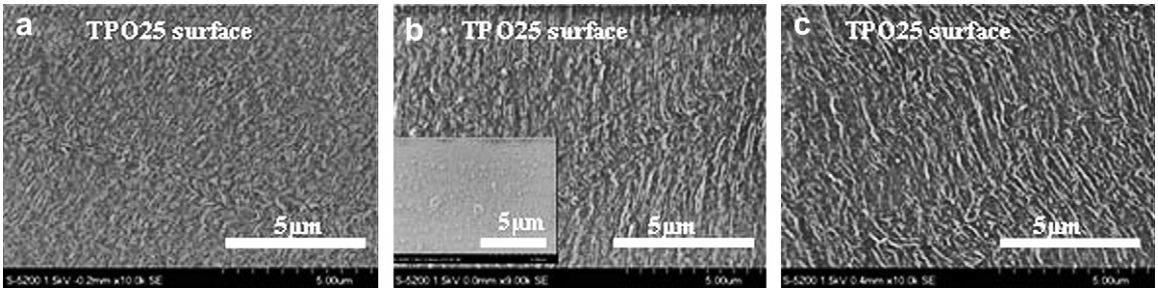

Fig. 5. SEM images of the top surface of solvent-etched (xylene, 99 °C) samples for V-TPO25 plaques (a) near the gate (b) in the center and (c) far from the gate. The inset in (b) shows the corresponding image of the surface prior to solvent etching.

a corresponding image of the original surface of the V-TPO25 plaque prior to solvent treatment. It shows that the surface of TPO plaque was essentially flat before etching. After solvent etching, one can see a much rougher surface, caused by the extraction of EBR. The magnitude of the roughness appears to increase from near gate to far from the gate. This result suggests that the size of the EBR features at or near the surface of the TPO increase from near the gate to far from the gate, influenced by the complex flow fields and the temperature gradient that accompany filling of the mold.

Some further details of the near-surface TPO morphology can be seen in Fig. 6, where we show SEM images, at two magnifications, of a center-cut region of two V-TPO25 samples that were sectioned parallel to the flow direction. One sample (a) was subjected to solvent etching with warm xylene. In addition to roughness caused by extraction of the more soluble EBR component, one can see lines extending parallel to the flow direction that are likely due to fiber-like crystalline iPP domains. Particularly interesting is the thin bright line at the sample surface. The other sample (b) was stained by exposure to RuO_4 vapors for 24 h. RuO_4 selectively stains amorphous domains in the sample and makes the crystalline morphology more prominent. At lower magnification, one also sees a sharp horizontal line near the top of the image representing the flat top surface of the sample. From RuO_4 staining alone, it is difficult to assign a chemical composition to this thin layer, but by comparing the two images in Fig. 6, one can imagine that this line represents a thin crystalline layer of iPP at the surface. Other authors [4,10] who have investigated TPO morphology have also found evidence for a thin iPP layer at the sample surface.

Underneath this layer, one sees evidence for lamellar domains oriented perpendicular to the surface (the transcrystalline layer), which can be seen more clearly in the inset at higher magnification. Many features of this structure are very similar to those seen in AFM studies of injection-molded iPP by Huy et al. [27]. Features similar to that seen in Fig. 6 are also seen in samples taken near and far from the gate.

To summarize, we see that the V-TPO set of samples have a pronounced skin layer, hundreds of micrometers thick, that is noticeably thinner far from the gate. Within the skin layer, one can see a pronounced transcrystalline layer. Solvent etching experiments indicate that significant amounts of EBR are present within the skin layer. A solvent-etched sample section, as well as a RuO_4-stained sample, both sectioned parallel to the flow direction, show a thin bright line at the sample surface, which is likely due to a very thin surface layer of iPP. Top-view images of solvent-etched samples show that EBR is present at or near the sample surface. Extraction of this component leads to significant roughening of the plaque surface, and the scale of the roughness increases with the distance from the gate. This result suggests that the EBR domains in the surface region of the sample are larger in size further from the gate. This may be associated with longer cooling times of the injection-molded polymer before it is quenched.

3.3. ATR-FTIR measurements of the surface composition of the TPO plaques

In order to explore what factors might be responsible for the position-dependent adhesion strength seen in the V-TPO12 samples, we carried out Attenuated Total Reflectance-Fourier Transform Infrared (ATR-FTIR) measurements to determine the surface composition of our injection-molded TPO plaques. These

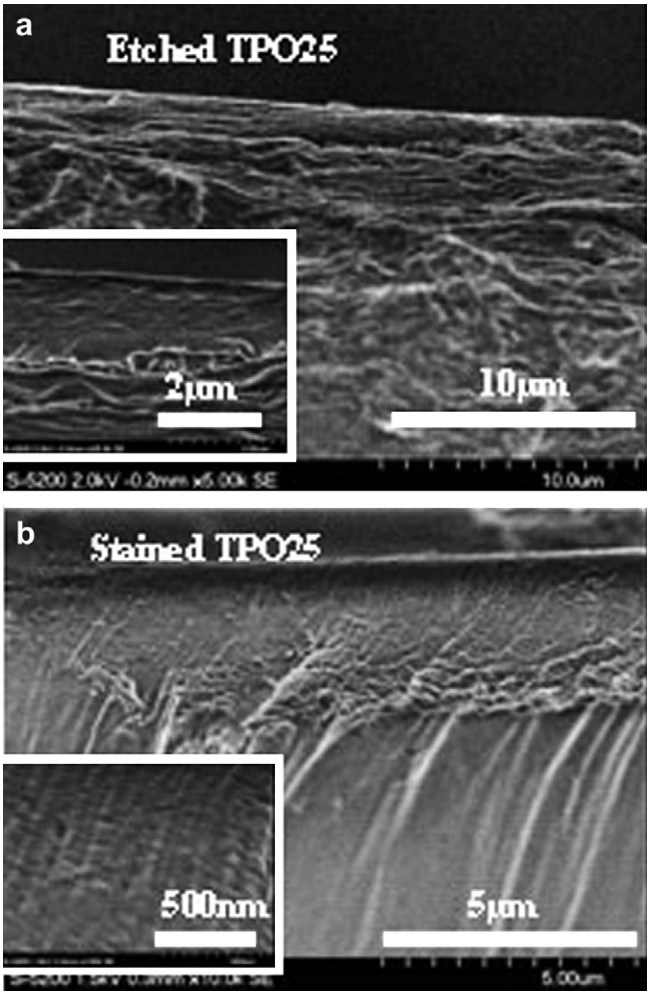

Fig. 6. SEM images of skin layer structure of the center section of a TPO25 plaque. The samples were cut in cross section before subjected to further processing. The top image (a) is of a sample that was solvent-etched (xylene, 99 °C) in a manner similar to that of the samples shown in Fig. 3. (b) is of a sample stained by exposure to RuO_4 vapors for 24 h. The inset is enlarged to higher magnification. The scale bars are indicated in each image.

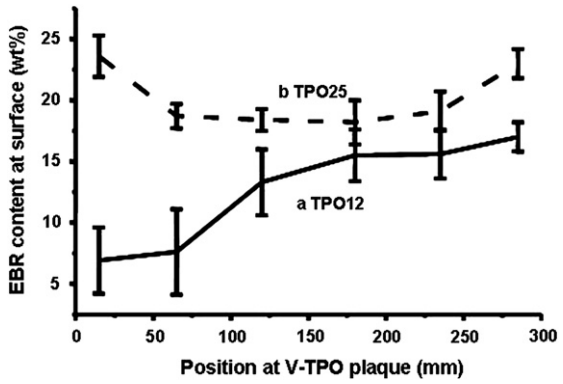

Fig. 7. EBR content determined by ATR-FTIR measurements for V-TPO plaque surfaces vs. distance from the gate.

measurements sample surface composition with a depth resolution of the order of 1 μm. We found that the intensities of several bands in the FTIR spectra, in the C–H stretching region between 3000 and 2800 cm^{-1}, and in the C–H bending region between 1500 and 1300 $cm^{-1}$of PP/EBR blends were dependent on the EBR content. Examples of the spectra and details of the analysis are presented in Supporting Information. The measurements were carried out on the same plaques used for the lap shear measurements. At least three specimens of each sample were tested. The results of these measurements are presented in Fig. 7.

While the V-TPO25 sample shows no significant variation in EBR content at the surface as a function of distance from the gate, the V-TPO12 sample is different. One can see that the ATR-FTIR measurements detect a significant variation in the amount of EBR at the sample surface. In the near gate region, the amount detected is somewhat lower (ca. 6 wt%) than the bulk (12 wt%) composition, whereas the EBR content of the surface regions becomes increasingly greater in the center and far from the gate portions of the sample. This variation is likely a reflection of both the flow fields and cooling rate associated with the injection molding of this plaque. This variation may have some relationship with the results obtained above for V-TPO25 plaques (Fig. 5) in which images of the solvent-etched plaque surface show significant roughening, and the scale of the roughness increases with the distance from the gate. By comparing the two curves in Fig. 7, we find that the EBR content at the surface of this V-TPO12 plaque in the near gate region is lower than that of our V-TPO25 plaque, while the EBR content at the surface of the V-TPO12 plaque in the center and the far from gate region is closer to that of the V-TPO25 plaque.

3.4. Relationship between the position and adhesion properties

In order to facilitate comparison of the lap shear fracture strength and adhesion energy with EBR9 content on the surface of TPO characterized by ATR-FTIR, the data in Figs. 4 and 7 were re-plotted in Fig. 8. One can see in Fig. 8A and B that the shapes of the solid curves, describing the fracture strength, resemble that of the dashed curves. Thus there appears to be a common trend, suggesting a possible relationship between adhesion and EBR content at the surface of TPO. Unfortunately, the changes in fracture strength with position are smaller than the error bars associated with the measurements. Fig. 8C and D shows the same trends, but the data for the change in fracture energy G_c as a function of position (i.e., as a function of EBR content in the near-surface region) are now outside of experimental error, at least to the level of one standard deviation.

Other factors than the EBR content in the near-surface region may also play a role in the change of adhesion energy with distance from the gate in the V-TPO12 plaque. For example, as shown in Table 1, the thickness of the skin layer of the TPO plaques decreased from the near gate region to the far from the gate region. This layer is still very thick (ca. 250–400 μm) compared to the depth sampled

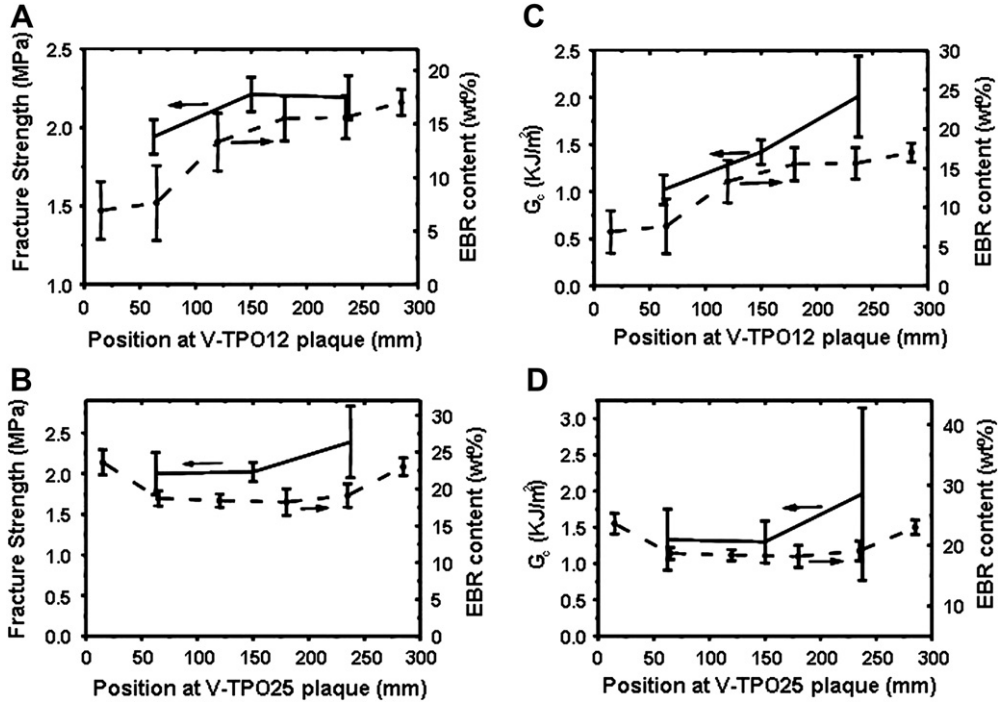

Fig. 8. Plots of the lap shear fracture strength and adhesion energy as a function of EBR9 content on the surface of TPO plaque vs. position at TPO plaque. A and C: TPO12 plaque, B and D: TPO25 plaque.

by ATR-FTIR, and it is unlikely to operate at the level of interpenetration of CPO and EBR molecules. It may, however, affect the local stiffness of the substrate, which in turn could affect the adhesion energy. We note, however, that no such effect was observed for the V-TPO25 plaque.

3.5. Fracture surface morphology

In this section, we examine the fracture surfaces following lap shear measurements on V-iPP and V-TPO samples. The images are presented in Figs. 9 and 10. One set of experiments employed laser scanning confocal fluorescence microscopy (LSCFM) and takes advantage of the fact that the CPO component is covalently labeled with a fluorescent dye. These are compared with scanning electron microscope (SEM) images, which provide much more detail about the fracture surface topography. This combination of methods is helpful for the determination of the locus of failure [28].

Fig. 9 shows the fracture surfaces of iPP/CPO/iPP, TPO12/CPO/TPO12 and TPO25/CPO/TPO25 symmetric lap shear joints. The substrates for these lap shear joints were taken from the central part of V-series plaques. The bright regions in LSCFM images correspond to the CPO layer, which contained a covalently bound fluorescent dye. The dark regions in these images correspond to substrate. The fracture surface of the iPP/CPO/iPP joint seen in Fig. 9a is bright and almost flat. The inset shows the opposite face of the fracture surface, which is smooth and dark. These images suggest that fracture involved interfacial failure at one of the CPO-iPP interfaces. The side-view image in Fig. 9d also shows a surface layer of CPO on top of the iPP substrate. While the bright layer shows some blemishes, it is relatively uniform in thickness. The corresponding SEM image in Fig. 9g shows a basically smooth CPO surface with a few irregularities caused by fracture. All these results are consistent with a predominance of interfacial failure as the fracture mechanism.

A fracture surface of a TPO12/CPO/TPO12 lap shear joint is shown in Fig. 9b. One sees a rough surface with bright regions and dark areas. The side-view image in Fig. 9e shows substantial distortion of the CPO layer and features that are much thicker than the CPO layer before fracture. The dotted lines in Fig. 9e and f indicate the position of the original surface of the TPO substrate. The SEM image in Fig. 9h shows fibrous features that suggest substantial deformation of material at the surface during failure. Similar features are seen in the corresponding images (Fig. 9c, f, and i) for the TPO25/CPO/TPO25 lap shear joint. Taken together, these

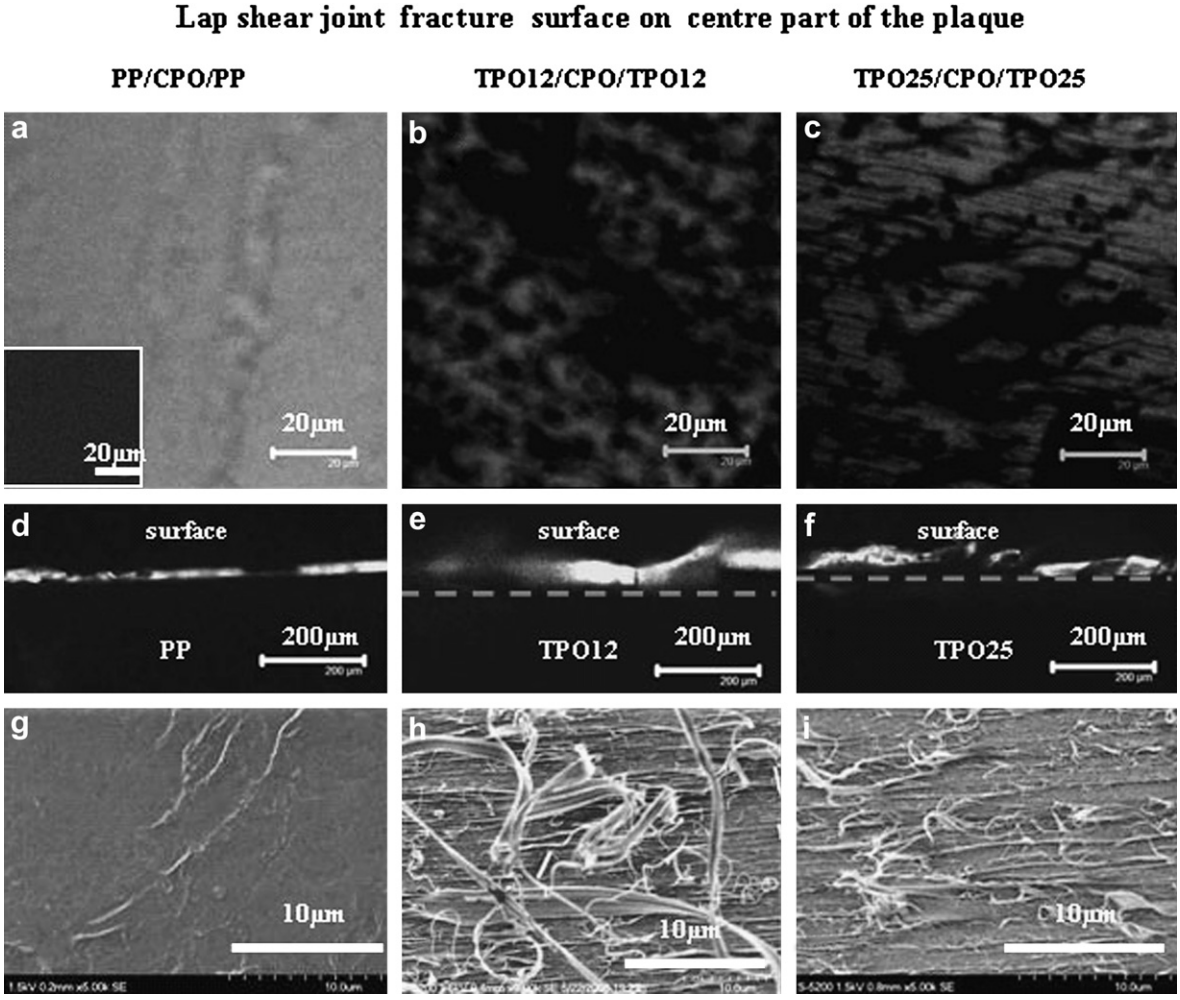

Fig. 9. The fracture surface of PP/CPO/PP, TPO12/CPO/TPO12 and TPO25/CPO/TPO25 lap shear joints. The substrates for the lap shear joints were taken from the central part of V-iPP or V-TPO plaques. (a), (b) and (c) are the LSCFM images of fracture surface (top-view). The brighter grey regions in LSCFM images correspond to dye-labeled CPO; the dark regions, to the iPP or TPO substrates. The inset in (a) is the opposite face of the fracture surface from (a). The uniform dark image of the inset indicates that there is no detectable CPO on this face of the fracture surface. Side-view LSCFM images of the fracture surfaces are presented in (d), (e) and (f). SEM images of the fracture surface are presented in (g), (h) and (i). The scale bars are indicated in each image.

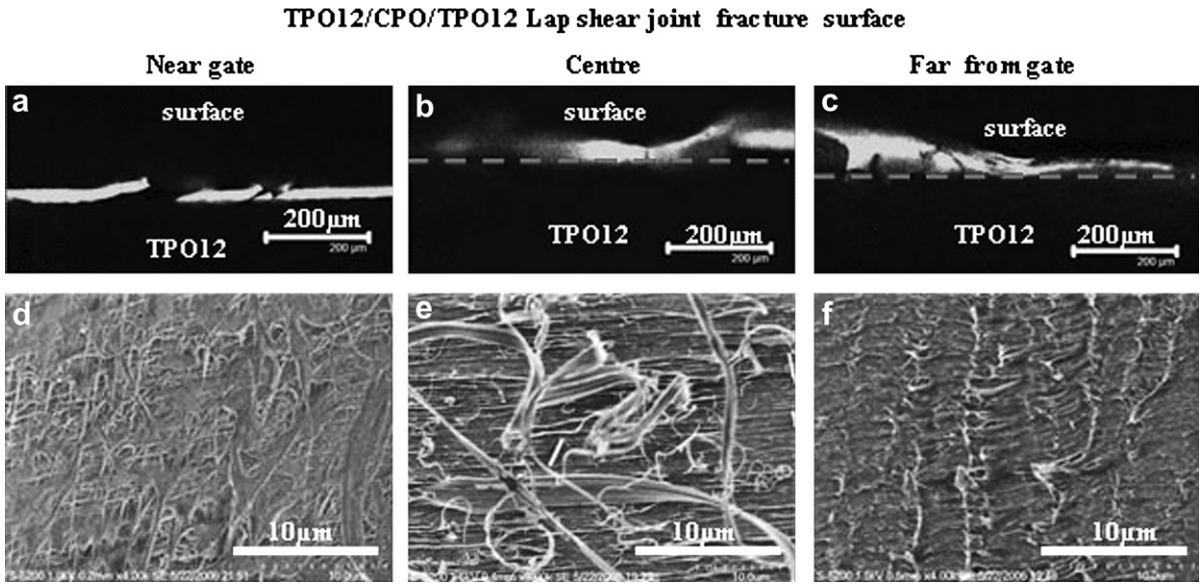

Fig. 10. The fracture surface of TPO12/CPO/TPO12 lap shear joint of the Visteon-made plaques. (a), (b) and (c) are the LSCFM images of fracture surface (side-view); (d), (e) and (f) are the SEM images of the fracture surface (top-view). The samples of (a) and (d) were taken from near gate plaques; the samples of (b), and (e) were taken from central plaques; the samples of (c) and (f) were taken from far from gate plaques. The scale bars are indicated in each image.

images show that during fracture, some parts of the TPO12 matrix or the TPO25 matrix were pulled away from the attached surface of the plaques. Fracture occurred both within the TPO substrate and in the CPO layer. These observations are consistent with a much stronger adhesion of CPO to TPO than to iPP.

Fig. 10 shows how the fracture surfaces of the V-TPO12/CPO/V-TPO12 joint varied with the position of the sample in the TPO plaque. Images of the fracture surface for the near gate region are shown in Fig. 10a and d. Here the CPO layer seen by LSCFM in the side-view appears reasonably uniform in thickness, interrupted by occasional sites of failure. The CPO-rich surface seen in the SEM image has small features associated with crazing and fiber formation upon fracture, but these features are smaller than those seen for fracture further from the gate. These images suggest that the mode of fracture here is a mix of interfacial failure and cohesive failure in the CPO phase. The images in Fig. 10b and e reproduce, for comparison purposes, the images in Fig. 9e and h from the center of the plaque. There is much more serious deformation of the CPO layer as well as the TPO surface compared to the near gate region. The deformation of the CPO layer in the far from the gate region, as seen in the side-view image in Fig. 10c is even larger than that in the sample cut from the center of the plaque. The corresponding surface SEM image is shown in Fig. 10f. We conclude that changes seen in the fracture surfaces generated failure in a lap shear test are consistent with differences in adhesion energy measured in those tests. Both of these changes appear to be due to the differences in the EBR content in the near-surface regions of the V-TPO12 sample as a function of the distance from the gate.

3.6. Relationship between composition to lap shear strength

The lap shear test results above showed that there is an increase in the fracture strength and much higher increase in adhesion energy with the increase of EBR9 content in TPO up to about 12 wt% EBR9. The data in Fig. 3 suggests that there is a small compensation accompanying a further increase in EBR content: the samples with 25 wt% ERB9 show greater strain at break but somewhat lower stress at break, so that little difference is seen in the calculated values of the adhesion energy. Here we consider factors that can affect the strength of adhesion in these samples.

Interfaces between different materials can be either sharp or diffuse, and fracture at these interfaces can be strictly interfacial, or cohesive, with crack propagation through the individual components on either side of the interface. There are normally two necessary and sufficient conditions for strong adhesion. The first, intimate molecular contact (wetting) at the interface is necessary to obtain strong interfacial attraction. Second, there must be chain interpenetration across the interface, preferably accompanied by molecular entanglements.

In our samples, when CPO was coated onto the surface of iPP or TPO plaque and the solvent was evaporated, the CPO molecules formed an intimate contact with the substrate. When the coated plaques were annealed at 120 °C, above the melting temperature of the crystalline phases of CPO and EBR9, the diffusivity of these molecules increased. We know from the work of Yin et al. [29] that for CPO/TPO25 samples, the interface width following the pre-bake in the Carver press was 21 ± 2 nm and that it broadened to 28 ± 2 nm upon annealing at 120 °C. In contrast, the interface between CPO and iPP was much thinner (15 ± 2 nm) and was not affected by annealing at 120 °C. Other experiments have shown that iPP is essentially immiscible with CPO [30]. These results are consistent with weak adhesion between CPO and iPP as well as with our observation of interfacial failure for this pair. Taken together, these results suggest that at the CPO/TPO interface, CPO chains penetrate into the EBR domains of the TPO. Upon cooling, one has the possibility of both entanglements and co-crystallization of these components. Both processes would lead to strengthening of the interface.

4. Summary

In the present study, we describe the influence of position and composition on the adhesion of CPO to injection-molded TPO plaques as investigated by a single lap shear test. The results show that in comparison with iPP itself, there is only a small increase in the fracture strength for TPO containing 12 and 25 wt% EBR9 as an impact modifier. Fig. 3A shows that the strain at break is much

smaller for the iPP/CPO/iPP joint than for the TPO/CPO/TPO joint. Thus, the former is characterized more as brittle fracture, while the TPO/CPO/TPO joint exhibits a more elastomeric fracture. The strength of the interaction between CPO and the substrate is better characterized by differences in adhesion energy than by the stress at break. One could also see a compensation in behavior between the TPO12/CPO/TPO12 joints and the TPO25/CPO/TPO25 joints, whereby the latter had a larger extension-to-break but a somewhat smaller strength at break, so that the calculated adhesion energies of the two sets of samples were very similar and within experimental error of each other. Previous studies have shown that this CPO sample is immiscible with iPP and the CPO/iPP interface is very narrow. In contrast, the CPO shows greater miscibility with EBR9 and with TPO containing EBR, with an interface thickness of the order of tens of nanometer. On this basis one expects strong adhesion between TPO and CPO than between iPP itself and CPO.

One of the most interesting findings reported here is that the adhesion energy of CPO with a TPO plaque (V-TPO12) increased with the distance from the injection molding gate. This increased adhesion was correlated with changes in the amount of EBR detected in the near-surface region of this TPO plaque by ATR-FTIR. Differences were also seen in the fracture surfaces as monitored by SEM and LSCFM. Ryntz [8–10] has argued that flow fields associated with injection molding of automotive parts affect not only the morphology of the TPO, but also the strength of the interaction of the adhesion promoter with the TPO substrate in these painted parts. Our results, for this V-TPO12 plaque, provide confirmation of this idea.

Acknowledgements

The authors would like to thank Visteon, E.I. DuPont Canada, NSERC Canada for financial support of this research, and China Scholarship Council (CSC)'s financial support. The authors are grateful to Drs. N. Coombs and I. Gourevich for help with the SEM and LSCFM experiments. We also gratefully acknowledge Professor C. Allen for providing access to her DSC apparatus and to Professor M.C. Goh for use of her optical microscope.

Appendix. Supplementary data

The supplementary data associated with this article can be found in the on-line version, at doi:10.1016/j.polymer.2009.08.027.

References

[1] Seki M, Vchida H, Maeda Y, Yamauchi S, Takgi K, Ukai Y, et al. Macromolecules 2000;33:9712–9.
[2] Yokoyama Y, Ricco T. Polymer 1998;39(16):3675–81.
[3] Lin YS, Yasuda HK. J Appl Polym Sci 1998;67:855–63.
[4] Tang H, Martin DC. J Mater Sci 2002;37:4777–85.
[5] Moffitt M, Yahya R, Chen W, Tong JD, Winnik MW, Thurman DW, et al. J Polym Sci Polym Phys 2002;40:2842–59.
[6] Tong JD, Moffitt M, Huang XY, Winnik MW, Ryntz RA. J Polym Sci Polym Chem 2001;39:239–52.
[7] Moffitt M, Rharbi Y, Li HX, Winnik MW. Macromolecules 2002;35:3321–4.
[8] Ryntz RA, Xie Q, Ramamurthy AC. J Coat Technol 1995;67(840):35–46.
[9] Prater TJ, Karberline SL, Holubka JW, Ryntz RA. J Coat Technol 1996;68(857):83–91.
[10] Ryntz RA. Prog Org Coat 1996;27:241–54.
[11] Mirabella FM, Dioh N. Polym Eng Sci 2000;40:2000–6.
[12] Yin Z, Ma Y, Chen W, Coombs N, Winnik MA, Ryntz RA, et al. Polymer 2005;46:11610–23.
[13] Tomasetti E, Legras R, Henri-Mazeaud B, Nysten B. Polymer 2000;41:6597–602.
[14] Morris HR, Munroe B, Ryntz RA, Treado PJ. Langmuir 1998;14:2426–34.
[15] Morris HR, Turner JF, Munroe B, Ryntz RA, Treado PJ. Langmuir 1999;15:2961–72.
[16] Ma YCh, Farinha JPS, Winnik MA. Macromolecules 2004;37:6544–52.
[17] Al-Harthi M, Kahraman R, Yilbas B, Sunar M, Abdul aleem BJ. J Adhes Sci Technol 2003;17(13):1831–45.
[18] Boiko Yuri M, Lyngaae-Jorgensen Jorgen. Polymer 2005;46:6016–24.
[19] Guerin G, Mauger F, Prud'homme RE. Polymer 2003;44:7477–84.
[20] Deng K, Winnik MA, Yan N, Jiang Z, Yaneff PV, Ryntz RA. Polymer 2009;50(14):3225–33.
[21] Brandrup J, Immergut EH, editors. Polymer handbook. 3rd ed. New York: Wiley; 1989. p. V19–29.
[22] Mencik Z, Fitchmun DR. J Polym Sci Polym Phys 1973;11:973–89.
[23] Matsumoto K, Miura I, Hayashida K. Kobunshi Konbunshu 1979;36:401–6.
[24] Fujiyama M, Wakino T. J Appl Polym Sci 1991;43:57–81.
[25] Fujiyama M, Wakino T. J Appl Polym Sci 1988;35:29–49.
[26] Ryntz RA, McNeight A, Ford A. Plastic Eng 1996;52(9):35–8.
[27] Huy TA, Adhikari R, Lüpke T, Henning S, Michler GH. J Polym Sci Polym Phys 2004;42:4478.
[28] Wu S. Polymer interface and adhesion. New York: Marcel Dekker, INC; 1982 [chapter 10].
[29] Yin Z, Yang J, Coombs N, Winnik MA, Ryntz RA, Yaneff PV. Polymer 2007;48:1297–305.
[30] Deng K, Felorzabihi N, Winnik MA, Jiang Z, Yin Z, Yaneff PV, et al. Polym Adv Technol 2009;20(3):235–45.